Soft Matter

Accepted Manuscript

This is an *Accepted Manuscript*, which has been through the Royal Society of Chemistry peer review process and has been accepted for publication.

Accepted Manuscripts are published online shortly after acceptance, before technical editing, formatting and proof reading. Using this free service, authors can make their results available to the community, in citable form, before we publish the edited article. We will replace this *Accepted Manuscript* with the edited and formatted *Advance Article* as soon as it is available.

You can find more information about *Accepted Manuscripts* in the Information for Authors.

Please note that technical editing may introduce minor changes to the text and/or graphics, which may alter content. The journal's standard Terms & Conditions and the Ethical guidelines still apply. In no event shall the Royal Society of Chemistry be held responsible for any errors or omissions in this *Accepted Manuscript* or any consequences arising from the use of any information it contains.

ROYAL SOCIETY OF CHEMISTRY

www.rsc.org/softmatter

ARTICLE TYPE www. rsc.org/xxxxxx | XXXXXXXX

Phase behavior of polyhedral nanoparticles in parallel plate confinement†

Mihir R. Khadilkar[*a] **and Fernando A. Escobedo**[b‡]

Received Xth XXXXXXXXXX 20XX, Accepted Xth XXXXXXXXX 20XX
First published on the web Xth XXXXXXXXXX 200X
DOI: 10.1039/b000000x

Monte Carlo simulations are used to investigate the phase behavior of hard cubes, truncated cubes, cuboctahedra and truncated octahedra when confined between two parallel hard walls. The walls are separated by a distance H* which is varied to accommodate a different number of layers, from a monolayer up to approximately 5 layers, hence allowing us to probe the transitional phase behavior as the system goes from a quasi-2D geometry to a quasi-3D bulk behavior. While our results do reveal some phases whose structures resemble those that have been observed before for such systems in 2D and 3D spaces, other phases are also detected, including buckled phases, rotator plastic phases, and solids with significant translational disorder. Ordered phases formed for H* values that are a little too narrow to accommodate an additional particle layer are particularly interesting as they tend to have complex structures. The maximum density for such frustrated phases is low compared to that of non-frustrated ones for the same system at different H*. As the asphericity in the shapes is reduced, the simulated phases show structural features that approach those of the phases that have been reported for hard spheres under similar confinement.

1 Introduction

Anisotropic colloidal nanoparticles have been receiving significant attention in the scientific literature due to both their importance as model systems to study various atomic phenomena and their potential for technological applications. Much of this interest has been fueled by the development of robust synthesis methods[1–7] and the ability to tailor and control various key properties like shape, size, and the type and strength of specific interactions. In particular, regular polyhedral nanoparticles have emerged as versatile building blocks which can be efficiently synthesized[8–10] and give rise to a diverse range of phases[11–19] due to their combination of shape anisotropy and rotational symmetry. Controlled assembly of these ordered structures is desirable in terms of technological applications, specifically towards tuning their structural, mechanical, electrical, photonic and dielectric properties.

Apart from the shape and interactions of the individual particles, phase behavior is also affected by a strong spatial confinement that would preclude bulk behavior to fully develop. In fact, both experimental[20–26], and modeling[27–31] studies have found new particle structures that only form under confinement. Apart from its effect on the packing of simple spherical particles, spatial confinement has been shown[32] to control the ordering in various other shapes including hard rods[33], spherocylinders[34], polygons[35–37] and spherical caps[38]. Spatial confinement poses an additional constraint on the assembly of particles, often giving rise to structural motifs not seen in the bulk. In the absence of any enthalpic interactions, when the ordering is driven only by entropic forces (which are constrained by the accessible space), the extent of spatial confinement molds the types of structures that maximize the total entropy. Even an exotic and elusive phase like a quasicrystal has recently been observed[39] using spatial confinement. Several established experimental techniques are routinely used wherein colloidal particles are confined to a few layers, thus giving rise to a range of phases depending on the extent of confinement[40–43]. Often, dense packings of confined colloidal particles are achieved by trapping the particles in a wedge geometry with a very small wedge angle, so that different sections along the plates can be approximated as parallel confinements. Some of these confined systems have been shown to have interesting tunable optical properties including photonic band gap[42,44,45] and the wedge geometry has been shown capable of stabilizing phases that would be unstable in the bulk case[46]. In this paper, we examine how spatial confinement affects the phase behavior of hard particles with selected polyhedral shapes from the truncated cube family[47]. A recent simulation study[48] explored the phase behavior of these shapes when pinned to a flat interface which mimics some experiments of particle assembly performed on a fluid-fluid interface. In that scenario, the centers of mass of the particles essentially exist on a 2D plane (even if particles can freely

† Electronic Supplementary Information (ESI) available: [details of any supplementary information available should be included here]. See DOI: 10.1039/b000000x/

[a] *Department of Physics, Cornell University, Ithaca, NY-14853 (USA).*
[b] *Department of Chemical and Biomolecular Engineering, Cornell University, Ithaca, NY-14853 (USA); E-mail: fe13@cornell.edu*

rotate). Our focus, however, is on *slit* confinement that allows for the formation of a few particle layers in between two hard walls; such a system allows bridging the gap between the known phase behaviors for such particles in 2D and in (bulk) 3D. The rest of the manuscript is organized as follows: in Section II we describe the models and methods used, in Section III we present our results, in Section IV we summarize the global trends in phase behavior, and in Section V we provide some concluding remarks. Additional complementary results are given in a supporting information file (SI)[49].

2 Shapes, Model and Methodology

Using Monte Carlo (MC) simulations, we studied four shapes from the truncated cube family[47] (see Figure 1) with increasing level of truncation, s (the precise definition of s is detailed in the Supplementary Information of Ref.[47]). Specifically, we studied perfect cubes (C) (s = 0), truncated cubes with s = 0.4 (TC4), cuboctahedra (CO) (s = 0.5) and truncated octahedra (TO) (s = 0.66). Spatial confinement was modeled by hard walls in the Z-direction, while periodic boundary conditions were used in the X and Y directions. Each shape was studied for a range of confinements, characterized by a non-dimensional height H* = H/ σ, where σ is the minimum distance between the hard confining walls that allows the particle to exist within the walls (in at least *one* orientation) without overlap with the walls. For C, TC4 and CO, σ is the edge-length of the equivalent cube that the shape is truncated from. For TO, it is the distance between the parallel opposing hexagonal faces. Lengths reduced by σ convey the maximum number of layers that a particular confinement value can potentially allow (barring buckled layers).

All shapes were treated as hard particles (with no enthalpic interactions), which amounts to disallowing any particle-particle or particle-wall overlaps (using the Separating Axis Theorem[50]). For each of the shapes, we simulated a system of 800 particles for a range of H* values (from H* = 1 to H* = 5). At high densities, our simulations spanned between 12 to 20 particle rows (depending on H*) along each of the X and Y dimensions to minimize finite-size effects. We also checked our results by performing simulations on larger systems (N = 2000). For a given H* value, MC simulations were carried out in a constant-pressure (NPT) ensemble, starting from low density liquid-like configuration and gradually compressing via small pressure steps. Each MC cycle consisted of N translation, N rotation and 2 volume move attempts. Each pressure step included 3×10^6 MC cycles for equilibration and 10^6 cycles for production. The volume moves affected the X-Y dimensions only and after the system ordered, were allowed to be triclinic (to relieve any remnant stress). In certain areas of the phase space where full equilibrium was suspect, we checked our results with longer MC runs (7×10^6 cycles per step).

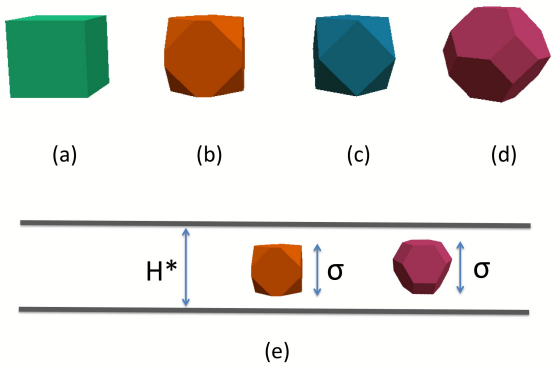

Fig. 1 Particle shapes studied in this work: (a) Perfect cube(C), (b) truncated cube with truncation parameter 0.4 (TC4), (c) cuboctahedra (CO) and (d) truncated octahedra (TO) and (e) a schematic of particles between two parallel plates illustrating parameters H* and σ.

2.1 Order parameters

We make use of several order parameters to track the formation of ordered phases. Because of the geometry of our system, the usual order parameters used for either 2D or 3D bulk systems are not directly usable and do not carry the same meaning in the current situation. Hence we use order parameters in a slightly modified form as specified below.

To track positional ordering, we used the Ψ_4 and Ψ_6 order parameters that are generally used in two dimensions to track square or hexagonal bonding symmetry, respectively. To calculate Ψ_4 and Ψ_6, we assign for each particle i, a complex number characterizing its local n-fold bond orientational order $\phi_n(\mathbf{r}_i)$:

$$\phi_n(\mathbf{r}_i) = \frac{1}{n_i} \sum_{j=1}^{n_i} \exp(in\theta_{ij}) \tag{1}$$

for n = 4 and 6. Here, θ_{ij} is the angle made by the virtual bond between particle i and its nearest neighbor j with respect to an arbitrary global axis, and n_i is the number of nearest neighbors of particle i. For n = 6, n_i is calculated via Voronoi tessellation, while for n = 4, the 4 closest neighbors are used for the calculation to avoid the degeneracy in Voronoi construction that can arise in such a case[51]. The global bond orientational order Ψ_n is calculated by:

$$\Psi_n = \left| \frac{1}{N} \sum_{i=1}^{N} \phi_n(\mathbf{r}_i) \right| \tag{2}$$

A key modification we make to the above definitions of ϕ_n and Ψ_n is that we first isolate single layers within the system (in case there are more than one), compute ϕ_n values from Eq. (1) using only same-layer nearest neighbors, and then calculate Ψ_n values for the set of particles in each layer. In case of multiple layers, we report the Ψ_n value averaged over all layers. We define the particles to be within a particular layer by specifying a suitable Z-coordinate range, such that particles define a layer parallel to the walls and exclude any buckling.

Additionally, we also use the Q_4 and Q_6 bond-order orientational parameters[52] to probe and monitor translational order. These parameters are defined as:

$$Q_l = \frac{4\pi}{2l+1}\left[\sum_{-l}^{+l}|\bar{Q}_{lm}(\mathbf{r})|^2\right]^{\frac{1}{2}} \tag{3}$$

where $\bar{Q}_{lm}(\mathbf{r})$ is given by

$$\bar{Q}_{lm}(\mathbf{r}) = \frac{1}{N_b}\sum_{bonds} Y_{lm}(\mathbf{r}) \tag{4}$$

where $Y_{lm}(\mathbf{r})$ are spherical harmonics for the position vector $\mathbf{r}$.

Like for Ψ_4 and Ψ_6, we also modify the definitions for Q_4 and Q_6 by restricting the summation to *non-interfacial* particles only (i.e., particles that are not in the layers closest to the walls).

Global orientational order is gauged by the cubatic order parameter[11] P_4, which is defined as:

$$P_4 = \max_n \frac{1}{N}\sum_i P_4(\mathbf{u}_i\cdot\mathbf{n}) \tag{5}$$

$$= \max_n \frac{1}{8N}\sum_i \left(35\cos^4\theta_i(\mathbf{n}) - 30\cos^2\theta_i(\mathbf{n}) + 3\right) \tag{6}$$

where $\mathbf{u}_i$ for i = 1, 2, and 3 denotes the unit vectors describing the particle orientation and $\mathbf{n}$ is a director unit vector that maximizes P_4. However, for shapes with flat faces in confined geometries, the director perpendicular to the walls tends to be associated with high P_4 values even in the presence of in-plane disorder. Hence, we also use the director with the second highest P_4 value (which is most orthogonal to the first director) as it seems to more reliably track in-plane orientational ordering.

Different phases are identified by analyzing the trends and features of the relevant order parameters and the equation of state as obtained from the compression runs. The phase diagrams for each of the shapes are obtained as a function of reduced pressure P* and volume fraction Φ. The reduced pressure P* is defined as $P^* = P\sigma^3/k_BT$ where σ is the length used for non-dimensionalizing H*, k_B is Boltzmann's constant and T is temperature.

3 Results

In our ensuing descriptions, we will focus on the ordered phases that form at high densities (above the disorder-to-order transition pressure) and hence we disregard the low-density isotropic fluid. Before describing results for specific particle shapes, we first outline some trends of behavior that are shared for all systems. In the absence of any enthalpic interaction, the assembly of the systems studied here is driven purely by entropy. Hence, the systems try to minimize their Gibbs free energy that, if not for a typically small PV contribution, essentially corresponds to maximizing the entropy for the given conditions (pressure and confinement). For a confinement which is equal to or slightly bigger than a length commensurate with N layers of the expected particle lattice arrangement (i.e., H* $\sim$ N), the configurations obtained under high compression are highly ordered and can attain density values near that of the densest bulk phase. However, when H* is slightly less than a whole number, the system cannot pack space efficiently, giving rise to relatively low densities at the most compressed state where the unused space allows some partial translational disorder. Further, such most compressed states having relatively low densities can produce structural motifs that would not be favored in the bulk systems. Overall then, H* controls the number of *layers* possible in the Z direction and the symmetry of the phases observed.

3.1 Cubes

We show in Figure 2 the broad trends in phase behavior for cubes in a volume fraction Φ *vs.* degree of confinement H* phase diagram. We observe a transition from a disordered fluid at low volume fractions (and low pressures) to a crystal with square or cubic order as the system is compressed. This behavior is similar to those observed in both bulk 3D systems and 2D hard squares[36]. For confinements approaching a single layer (H*$\rightarrow$ 1), we see regions which have significant particle orientational order and intermediate four-fold bond-orientational order (gauged by Ψ_4), suggestive of tetratic-like order. The Ψ_4 value for these confinements increases continuously with pressure, giving way to a square order (see Figures S1 and S2 in the SI[49]).

In the entropy-driven self-assembly of cubes, one observes cubic crystalline ordering at sufficiently high Φ. However, such perfect ordering requires commensurability between lattice spacing and the available space (in the simulation box). Under slit confinement, that requirement is not always satisfied along the Z axis. Hence the phase that maximizes the entropy at high Φ is not necessarily a perfectly ordered cubic phase due to the extra space resulting from the incommensurability.

The dependence of phase behavior and multilayering on H*

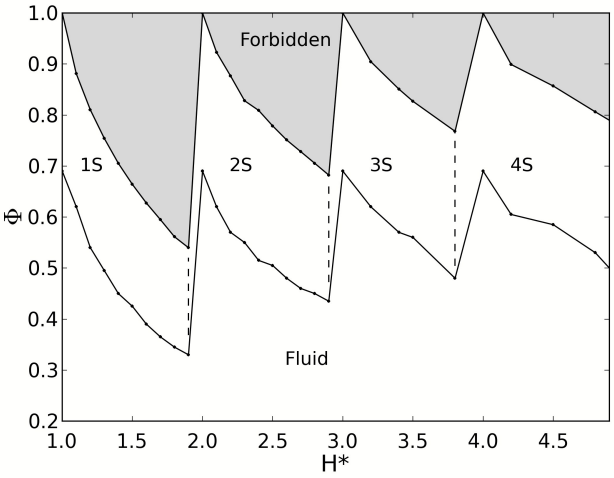

Fig. 2 Phase diagram of cubes as a function of volume fraction Φ and confinement H*. The phase boundaries marked here are only approximate; in particular, the isotropic-solid two-phase regions are depicted by lines.

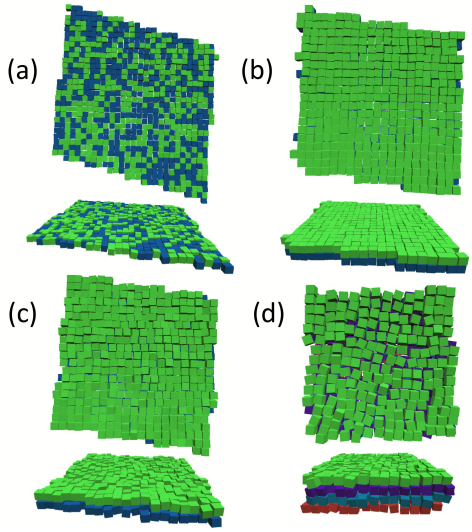

Fig. 3 Snapshots (top-down and side views) depicting the structure of cubes at representative confinement values (a) 1S phase at H* = 1.5 at $\phi \approx 0.61$ (b) 2S phase at H*= 2.1 at $\phi \approx 0.85$, (c) 2S phase at H* = 2.9 at $\phi \approx 0.62$, (d) 4S phase at H* = 4.8 at $\phi \approx 0.52$.

can be illustrated over different H* ranges (see Figure 3 for a range of sample snapshots). For example, up to H* = 1.9, there is space only for a single layer. So for confinements in the range $1.1 < H^* < 1.9$, the *free volume* available around the layer increases with H*, which leads to higher misalignment (in the Z-direction) as we increase H*. This can be explained by the fact that when the space available is not enough to accommodate another layer, the system maximizes entropy by exploring the configurational freedom available in the Z-direction (which leads to misalignment).

As we go from H* = 1.9 to H* = 2.1 (thus increasing a layer), the packing becomes abruptly more efficient. With more than one layer, one can also envision displacement modes wherein one layer *slides* over another. However, we did not observe any significant inter-layer displacement. This could be in part due to the fact that displacement modes in the Z-direction have to be coordinated within and across layers and inter-layer sliding (on the XY plane) would prohibit this entropic freedom. Within a single layer regime (say, $2 < H^* < 3$), it is the size and extent of these displacements that characterize the phase behavior since the number of layers remains the same.

We can visualize the misalignments in the Z-direction by plotting the center-of-mass particle density distribution along the Z-coordinate (See Figure 4) for various confinement widths at the lowest ordering pressures (i.e., at the isotropic-solid phase boundary). Interestingly, the Z-distributions, which are unimodal for $H^* < 1.6$ or so, turn bimodal, for $H^* \geq 1.6$ (for high enough volume fractions), although there is not enough space for a separate layer. In some cases (like for H*=1.6), the Z-distributions turn bimodal only at high volume fractions. As we can see in Figure 4, the misalignment, that can be quantified as the *spread* of the distribution (as measured by the standard deviation), increases continuously from about 0.02 at H* = 1.1 to about 0.3 at H* = 1.9. After addition of another layer, misalignment again drops to 0.04 at H* = 2.1 and starts increasing again with H. Although the H* = 1.9 phase shows a bimodal Z-particle distribution, the particles associated with the two peaks do not exhibit local spatial correlations and hence it is not classified as a buckled phase.

The ordered phase near the order-disorder concentration in 3D bulk has been associated with a cubic mesophase (due to high particle mobility)[11–13] or with a cubic crystal with an unusually large amount of vacancies[53]. The behavior of such low-density ordered-phases appears to be somewhat distinct in our confined systems, especially for those H* values that are a little too narrow to accommodate an additional particle layer and hence have very low Φ and can host the largest amount of vacancies (e.g., the system for H* = 4.8 and Φ = 0.52 shown in Fig, 3d). Unlike the bulk system, vacancies now do not seem to distribute isotropically but concentrate along the Z axis. The broad spread of the Z-axis particle distribution (as in Fig. 4d) could be seen as an indicator of translational disorder, hence making such states unusual solid phases (even mesophases). In fact, significant translational disorder can also be observed in the X-Y planes (see e.g., the top-down view in Fig. 3d), although this may be a finite size effect[53]. Alternatively, such misalignments could be seen as local dis-

placement modes akin to (unusually large) phonons in a perfect crystal; phonon modes have been shown to be important contributors to the free energy of hard-core ordered phases (see, e.g.,[54]). Either way, such structures are rather unique and while some taxonomy could be implemented (e.g., based on a metric of translational Z-axis fluctuations) to mark their presence as distinct phases in Fig. 2, we do not attempt this here and simply note that such Z-axis particle fluctuations persist even at high concentrations (for particular values of H*).

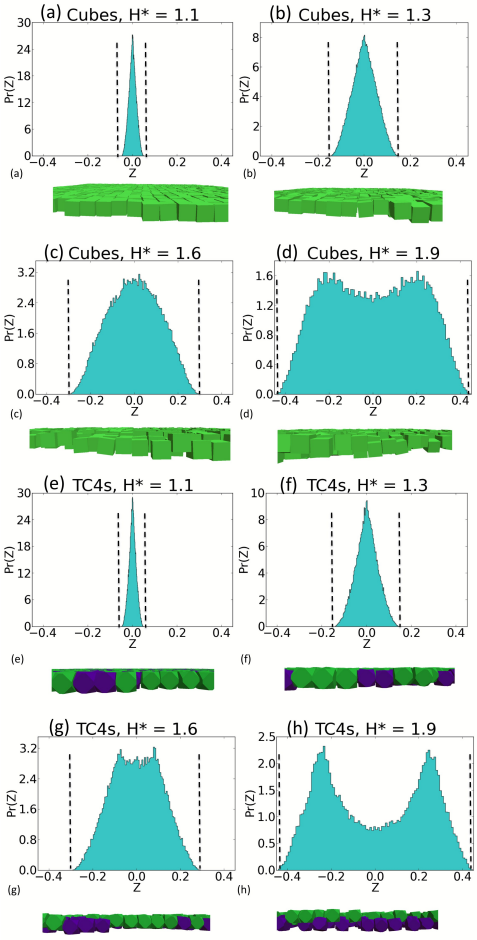

Fig. 4 Z-coordinate particle distribution at various confinements for cubes and TC4s at the lowest pressure where the ordered phase occurs. Accompanying snapshots for each case show the extent of misalignment in the Z-direction. Dotted lines indicate the physical bounds of the space that a particle center of mass can span for the given H* value. Different colors indicate whether the particle is above or below the mean Z-coordinate.

Overall, the phase behavior we observe for cubes in slit confinement for H* < 2 is broadly similar to those observed in earlier studies of squares in 2D[36] and of freely rotating cubes whose centers are restricted to lie on a flat interface[48]. However, crucial differences emerge from the fact that slit confinement results in more extra space available as layer spacing incommensurability increases, which results in particle in-plane misalignment and displacement modes akin to phonons in bulk crystal.

3.2 TC4

TC4 is a truncated cube with 80% of its corners cut off (s = 0.4). We chose this shape since it has been shown to exhibit a mesophase behavior[47] in 3D bulk systems that is significantly different from that of either cubes (s=0) or cuboctahedra (s=0.5).

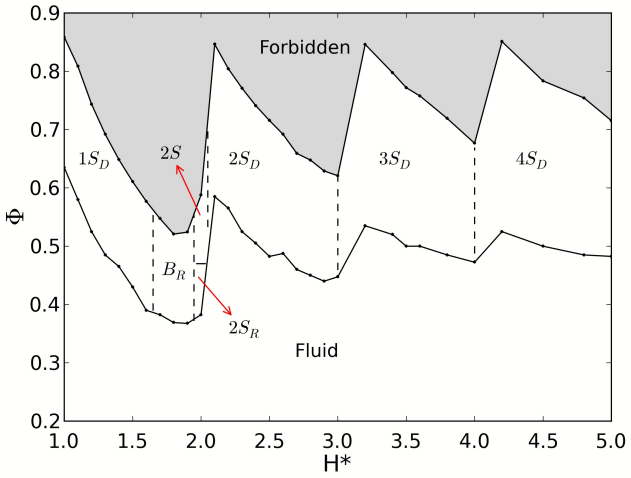

Fig. 5 Phase diagram of TC4 as a function of volume fraction Φ and confinement H*. The nomenclature for the phases is as follows: the number represents the number of layers; S or S_D represent square and distorted square phases respectively while B_R and S_R represent buckled rhombic phase and square rotator phase, respectively. The phase boundaries marked here are only approximate.

For TC4s we observe a phase behavior whose broad features are similar to those of cubes as Φ increases: a disordered fluid giving way to a distorted square crystal (see Figure 5) and decreasing concentrations at the isotropic-solid phase boundary and at the densest state within a particular H* range associated with an integer number of layers. However, between H* = 1.9 and H* = 2.1 we see different phases altogether.

Near H* = 1.9, we see a buckled rhombic phase ($1B_R$), wherein the particles get subdivided into either being close to the upper or the lower wall. This is reflected in the Z-coordinate distribution (see Figure 4). They still do not have enough space to form a separate layer (nearest neighbor particles tend to be at different heights in the Z-direction), and hence they form an imperfect buckled phase with rhombic

bond-orientational order (see Figure 6b). We note that we identify a buckled phase by a combination of a bimodal Z-distribution and snapshots of the system (like in Fig. 6b) that reveal the presence of spatially correlated rows of particles at different heights. Together, they are complementary indicators of a system frustrated between configurations involving complete layers.

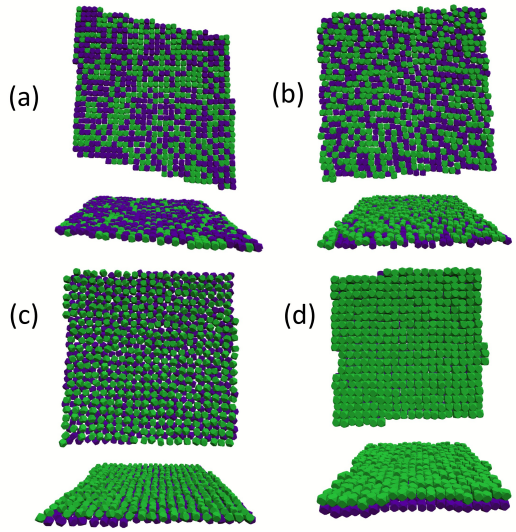

Fig. 6 Snapshots (top-down and side views) depicting the structure of TC4s at representative confinement values: (a) Single layer distorted square ($1S_D$) phase at H* = 1.5 and $\phi \approx 0.55$, (b) Buckled rhombic (B_R) phase at H*= 1.9 and $\phi \approx 0.46$, (c) Two-layer rotator square ($2S_R$) phase at H* = 2.0 and $\phi \approx 0.46$, (d) Two-layer distorted square phase ($2S_D$) at H* = 2.9 and $\phi \approx 0.57$. Particles are colored for ease of visualization and identification of layers only.

In contrast, at H* = 2.0 when the confinement width is enough to allow two separate layers, we see the formation of a two-layer square rotator ($2S_R$) phase (between $\Phi = 0.39$ to 0.47), eventually giving way to a two-layer square (2S) phase. The rotator phase is characterized by a reduced orientational order despite strong positional order. Above $\Phi = 0.47$, the system attains moderate orientational order, although some particles are still not oriented parallel to the wall (see Figure S4 in the SI[49]).

As we go beyond H*= 2.0, the only ordered phase we encounter has layers with a distorted square symmetry, with all particles oriented parallel to the wall (no rotator phase is detected). The phase behavior follows an overall trend of decreasing densest packing until an extra layer can be added, which results in a jagged upper phase boundary similar to that seen for cubes. Although TC4s in the bulk exhibit a rotator mesophase near the isotropic-solid transition, we did not observe a mesophase over the upper range of H* values studied here. This is likely due to having an insufficient number of layers in the Z-direction to approach bulk 3-D behavior.

3.3 Cuboctahedra (COs)

We also examined COs (s = 0.5) which, like TC4s, also show a rotator mesophase in their bulk 3D phase behavior[12,47].

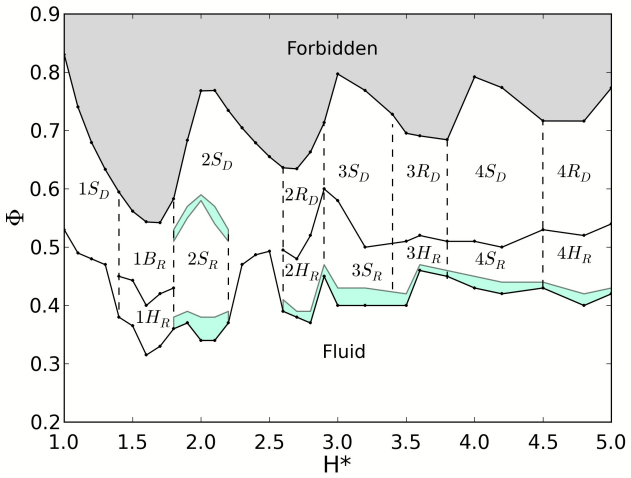

Fig. 7 Phase diagram of CO as a function of volume fraction Φ and confinement H*. Green shaded areas represent two-phase coexistence regions. Vertical dashed lines give approximate locations of phase boundaries.

Compared to TC4 or cubes, we observe for COs a rather different and richer phase behavior (see Figure 7 and 8). For small confinements ($1 < H^* < 1.5$), we observe a distorted square phase just like TC4 and cubes. However, for $1.5 \leq H^* < 1.7$ we see a hexagonal rotator phase ($1H_R$) leading to a buckled rhombic ($1B_R$) phase at higher Φ, similar to that seen for TC4s (see Figure 4). A hexagonal rotator phase, that acts as a precursor to the $1B_R$ phase, contains particles with a significant six-fold bond-orientational order (Ψ_6) while having little or no global orientational ordering (see Figure S5 in the SI[49]). At high volume fractions, the particles in the $1B_R$ phase exhibit some segregation along the Z-coordinate, without the formation of a separate layer akin to the behavior of the $1B_R$ phase in TC4s (see Figure 9 a-d).

For $1.8 \leq H^* < 2.3$, we again see a square rotator ($2S_R$) phase which upon compression leads to a 2-layer distorted square ($2S_D$) phase (see Figure 8 b). The $2S_R$ phase is stable for a large range of volume fractions (e.g., for $0.38 < \Phi < 0.58$ when H* = 2). For $2.3 \leq H^* < 2.6$, we do not observe a rotator mesophase, although we detect the formation of a distorted square phase ($2S_D$) similar to that observed for smaller H* values.

For $2.6 \leq H^* < 3.0$, we see a hexagonal rotator phase, $2H_R$

(a phase with six-fold bond orientational order but without global particle orientational order), that gives way to a distorted rhombic phase ($2R_D$). In this case, while the first transition (isotropic to $2H_R$) is seen to be discontinuous, the second transition ($2H_R$ to $2R_D$) appears to be continuous (see Figure S6 in the SI[49]).

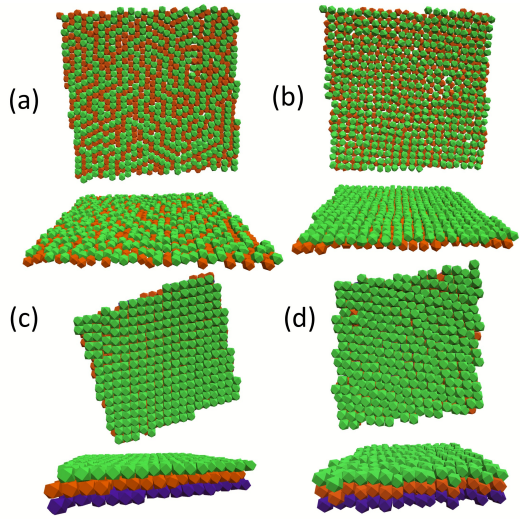

Fig. 8 Snapshots (top-down and side views) depicting the structure of COs at representative confinement values: (a) Buckled rhombic ($1B_R$) phase at H* = 1.7 and $\phi \approx 0.48$, (b) Two-layer rotator square ($2S_R$) phase at H* = 2.0 and $\phi \approx 0.69$, (c) Three-layer distorted square phase ($3S_D$) at H* = 3.2 and $\phi \approx 0.68$, and (d) Three-layer distorted rhombic phase ($3R_D$) at H* = 3.8 and $\phi \approx 0.60$. Particles are colored for ease of visualization and identification of layers only.

Between both $3 < H^* < 4$ and $4 < H^* < 5$ we see a recurring trend in the phase behavior. Within each of these regions, for small values of H* the isotropic phase transitions into a square rotator phase S_R, which has layers with high Ψ_4 values, that upon further compression goes into a distorted square (S_D) crystal. For larger values of H*, however, the isotropic phase transitions into a hexagonal rotator phase H_R that upon compression gives way to a distorted rhombic crystal (R_D). This change is likely due to differences in the availability of space in the Z-direction associated with H*. In the $3 < H^* < 3.4$ and $4.0 < H^* < 4.5$ ranges, the space is almost commensurate with a cubic-like ordering, leading to high four-fold bond orientational ordering. In the $3.4 < H^* \leq 3.9$ and $4.5 < H^* < 5.0$ regions, the extra space is not enough to accommodate an extra layer, but is large enough to significantly modify the preferred particle structural arrangement.

Overall, we see a larger variety of phases in COs compared to cubes or TC4s. While the buckled and square rotator phases are also observed for TC4s, only COs give rise to the distorted rhombic (R_D) phase and hexagonal rotator (H_R) phase. COs are also able to arrange into distinct structures in the regions where the extra space in the Z-direction is relatively large but insufficient for an extra layer.

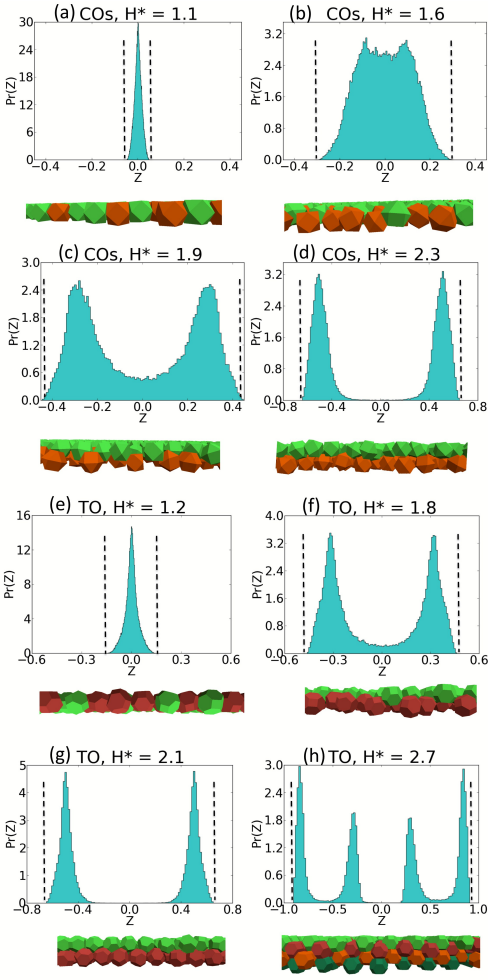

Fig. 9 Z-coordinate particle distribution at various confinements for COs and TOs. Except for TOs at H*=2.3, all plots are at the lowest pressure where the ordered phase occurs. Accompanying snapshots for each case show the extent of misalignment in the Z-direction. Dotted limiting lines indicate the physical bounds of the space that a particle center of mass can span for the given H* value. For TOs at H* = 2.7, the distribution correspond to $\Phi = 0.50$ where the $2B_S$ phase forms. Additional plots at lower Φ are given in Figure S9 in the SI[49].

3.4 Truncated Octahedra (TOs)

All the particle shapes studied so far are largely 'cube-like' and hence form cubic or distorted cubic lattices at high densities in the 3D bulk state[16]. TOs form a space-filling BCC lattice in bulk 3D conditions. Among the shapes studied, TOs have the largest truncation parameter (s = 0.66) and the small-

est asphericity.

A distinctive feature of a cubic or distorted cubic lattice is that it can be seen as the stacking of parallel layers of particles. This is important in a confined slit-geometry since the confining walls introduce fixed dividing planes which can predetermine the orientation of the particle layers of a (near) cubic lattice. For the BCC packing of TOs, however, any planar cut to the lattice leaves gaps in the lattice, thus leading to inefficient packing. This can be clearly seen from the maximum volume fractions (achieved in our MC compression simulations), that are significantly lower than not only unity but also those achievable for cubes (which are also space-filling in the bulk).

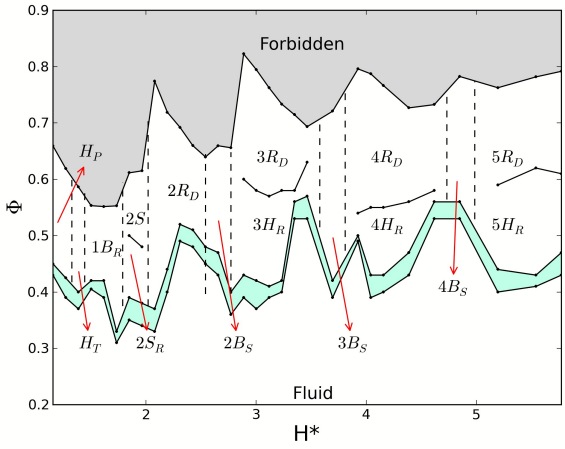

Fig. 10 Phase diagram of TO as a function of volume fraction Φ and confinement H*. Green shaded areas represent two-phase coexistence regions. Vertical dashed lines give very approximate locations of phase boundaries.

An important difference between TOs and other shapes relates to the particle orientations when the closest approach between two particles occurs, which is also the shortest width of a particle. For cubes, TC4s and COs such a distance is the edge-length of the cube they were truncated from (and hence the distance between opposing square faces). However, for TOs, this minimal distance is that between opposing *hexagonal* faces. This means that for the smallest values of H* studied (≈ 1.2), TOs tend to be aligned such that the hexagonal faces are parallel to the wall. We call this structure a H_P phase, denoting a phase with hexagonal bond-order and with the hexagonal face *parallel* to the walls (see Figure 10). For H* = 1.4, however, we see the H_T phase which also has hexagonal bond-order (with high values of Ψ_6), but the hexagonal face is *tilted* with respect to the wall. This is because, with the availability of more space in the Z-direction, TOs can increase their configurational entropy by exploring more particle orientations.

A set of snapshots depicting representative phases is given in Figure 11. For $1.4 < H^* \leq 1.7$, we see a buckled rhombic ($1B_R$) phase that is similar to those observed for the previous shapes. For ($1.7 < H^* < 2.0$), we see a familiar two-layer square rotator ($2S_R$) phase that eventually goes into a square phase ($2S$) upon compression. For ($2.1 \leq H^* < 2.6$), we see a single transition leading to a two-layer distorted rhombic ($2R_D$) phase, that has high Ψ_6 bond-orientational order and high global orientational order (see Figures S7 and S8 in the SI[49]). We get complementary information about the layering and translational order of these phases along the Z-axis from their Z-coordinate particle distribution (see Figure 9 e-h).

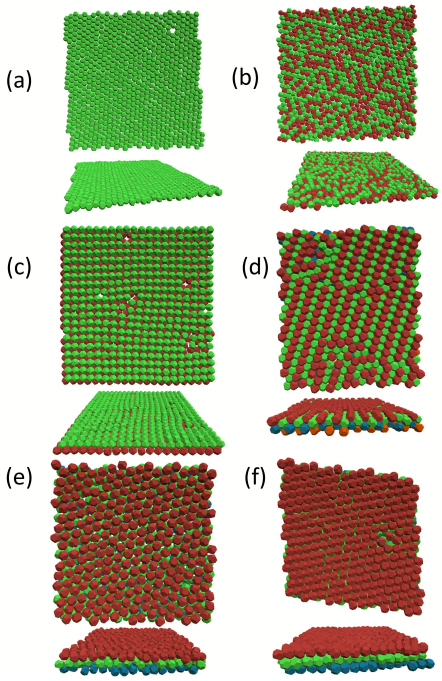

Fig. 11 Snapshots (top-down and side views) depicting the structure of TOs at representative confinement values: (a) Hexagonal parallel (H_P) phase at H*=1.2 and $\phi \approx 0.53$, (b) Buckled rhombic ($1B_R$) phase at H* = 1.6 and $\phi \approx 0.56$, (c) Two-layer rotator square ($2S_R$) phase at H* = 1.9 and $\phi \approx 0.66$, (d) two-layer buckled square ($2B_S$) phase at H*= 2.8 and $\phi \approx 0.67$, (e) three-layer hexagonal rotator ($3H_R$) phase at H*= 3.3 and $\phi \approx 0.51$, (f) three-layer distorted rhombic ($3R_D$) phase at H*= 3.3 and $\phi \approx 0.64$. Particles are colored for ease of visualization and identification of layers only.

For $2.6 \leq H^* < 2.9$, we see a phase not seen for other shapes, that has local coordination similar to the BCC structure of bulk TOs, but it has the 111 plane of the putative BCC structure parallel to the wall. This creates hills and trenches in the structure near the wall where TOs cannot pack space efficiently. Thus, the particles separate into *four* different sets of

heights along the Z axis, even though there is space for two full *nominal* layers only (see Figure 9 h). Such an arrangement is similar to the buckled phase seen for smaller H* values, except that it now has two full layers. Also, instead of the rhombic order previously detected in buckled phases, this phase has layers with a square order (with inner-layer particles possessing BCC-like local bond coordination as detectable by the Q_4 and Q_6 order parameters; see for example Figure S10 in the SI[49]). We will refer to this phase as a two-layer buckled square phase ($2B_S$) although a different acronym could be more informative (e.g., one that incorporates its interlayer BCC symmetry). Since we obtain the phase behavior primarily from compression runs, we see grain-boundary defects in the $2B_S$ ordered phase which do not easily anneal away even after longer compression runs.

For H* > 3.0, we first see the formation of a hexagonal rotator phase, $3H_R$ (having high Ψ_6 order parameter but little or no global orientational order), that upon further compression changes into a distorted rhombic phase (R_D), with the number of layers increasing with H*. In a small window after H*> 3.5, we observe a buckled square phase ($3B_S$) once more, but now with additional layers. For H* > 3.9, we again see the $H_R \rightarrow R_D$ transition seen before for $3 <$H*< 3.5. Near H* $\approx$ 4.8, we once more see a buckled square phase, but now with 4 *nominal* layers ($4B_S$). Importantly, the $3R_D$ and $4R_D$ phases also possess a BCC character as seen in their Q_4, Q_6 values (see Figure S11 in SI[49]). One could then say that the B_S type of phase arises when (due to the layer commensurability with H*) a BCC structure fits into the slit so that hexagonal facets of the TOs lie parallel next the walls (see, e.g., Fig. 11d), while the $3R_D/4R_D$ type of phase arises when the BCC structure now fits with hexagon-hexagon edges of the TOs pointing towards the walls (see, e.g., Fig. 11f). It is unclear for how long these $R_D \leftrightarrow B_S$ reorientation transitions of the BCC structure (with respect to the wall planes) will keep occurring as H* increases (for high Φ), or whether one of such orientations will become dominant as the bulk behavior ensues. In either case, the densest packings we observe are not close to 1 (as they would be for the space-filling phase in the bulk), but they steadily increase as the confinement is reduced.

Overall, the distinctive features of the phase behavior of TOs are likely due to their high truncation parameter (that makes them significantly different than cubes) while having low shape anisotropy (and low asphericity). The buckled square phases ($2B_S$, $3B_S$ and $4B_S$) are unique to TOs and appear when the BCC motifs (that TOs would favor in the bulk) can fit inside the slit in a particular orientation. We note, however, that the $2B_S$ and $3B_S$ phases tend to pack particles much less efficiently than the neighboring R_D phases (as seen in the *low* density they attain under maximum compression), and hence are favored only for small windows of H* in the range of H* examined. This may be the reason why we do not observe a $1B_S$ phase for very narrow slits. Also noteworthy is that certain confinements cause TOs to form dense structures quite dissimilar from their preferable bulk BCC packing, such as a two-layer square rotator phase ($2S_R$).

4 Remarks on global trends

In an attempt to consolidate our main results and to detect any broad trends in phase behavior across the different particle shapes that we studied, a global albeit qualitative phase diagram is constructed in Figure 12. We use the asphericity parameter (A) as a way to approximately rank the shapes (noting that low values are useful to identify particle shapes prone to exhibit rotator phases[12]). We adopt here the following definition:

$$A = 1 - \frac{S^*}{S} \tag{7}$$

Where S is the surface area of the actual particle shape and S^* is the surface area of the sphere having the same volume as the particle (A is closer to zero for a more sphere-like shape). We note that for the four particle shapes studied A and s (the truncation parameter) exhibit the opposite trends; i.e., larger s values correspond to smaller A. In the A vs. H* phase diagram (for $1<$ H* < 5) of Figure 12, besides the 4 shapes studied in this work we also include data for hard spheres from Ref.[30] to illustrate the limiting case of particles with no asphericity.

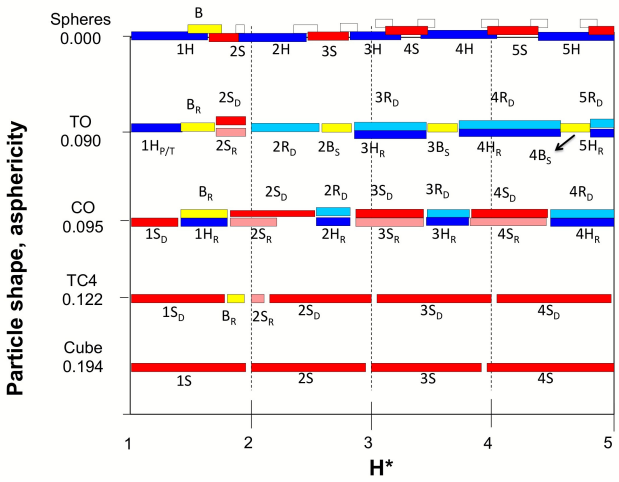

Fig. 12 Qualitative summary phase diagram of main ordered phases encountered in different confined polyhedra of the truncated cube family with different asphericity A values (A=0 corresponds to hard spheres) and different separations (H*). For any given A, each colored bar represents a phase with the bar appearing lower (higher) corresponding to the ordered phase occurring at lower (higher) volume fraction. For hard spheres, while bars represent intermediate phases of complex or mixed character.

Note that for hard spheres the lack of orientational order renders some of our phase classification superfluous; e.g., phases S_D and S_R simply become S. For hard spheres, however, we do not include all the phases that have been identified; in particular, intermediate phases that have a complex structure have been left as white bars. In Figure 12, similar colors are used to represent phases with similar structure (primarily in terms of translational order) regardless of number of layers; for example, light and dark red bars are for phases with layer of square bond order symmetry while light and dark blue bars are for phases with layers of hexagonal symmetry. For a given color type, the use of a darker/lighter shade is intended to convey the strength of the symmetry; e.g., a darker red has a stronger square symmetry than a lighter red. The following approximate trends are observed:

- As asphericity decreases, there is an increasing proclivity for phases with layers with hexagonal bond-order symmetry (in dark and light blue) to appear, taking over H* areas that (at low A) were occupied by phases with square bond-order symmetry (in dark and light red).
- As asphericity decreases, the number of layers that can fit in the channel (for a given H*) increases; e.g., 4-layer phases can occur even for $H^* < 4$.
- As asphericity decreases, the tendency for intermediate phases (occurring in between n and n+1 layered phases and between hexagonal and square bond order symmetry) increases.
- As asphericity decreases, the differences between a rotator and the non-rotator version of the same phase (of similar translational ordered) expectedly diminishes.
- One-layer buckled phases seem to be favored in systems with medium to low asphericities; if fact, it occurs for all systems except for cubes.

Along the asphericity axis of Figure 12, the transition from CO to TO to sphere phases is not gradual. In some respects, the phases in COs would seem to more closely correspond to the phases in the spheres (e.g., the alternation of phases with square and hexagonal symmetry with increasing number of layers as H* increases). Despite having a slightly lower asphericity than COs, TOs seem less prone to form layered phases with square symmetry. This illustrates that, expectedly, asphericity alone is not a complete descriptor of phase behavior (just as is case in the bulk) and that the particular way how certain shapes pack affects the types of symmetries that are favored. For instance, TOs show a preference for their (bulk) space tessellating packing, with the $2B_S$ and $3B_S$ phases being detected only for this particle shape.

Finally, we can also compare these results to previous calculations for polyhedra confined to a surface[48]. In the region $1 < H^* < 1.8$ or so, our system provides only enough room in the Z-direction for the particles in a monolayer to undergo rotations; such *narrow-slit* constraints can be conjectured to be *similar* to the *flat-interface* constraints for a monolayer system where the center of mass of the particles are confined to a stay on a flat surface. We indeed see a similar behavior for cubes in both scenarios. For TC4s on a flat interface, structures with both six-fold and four-fold orientational order were observed[48] as intermediates between the liquid and crystal phases. In our case, six-fold ordered structures are absent but we observe a buckled rhombic ($1B_R$) phase that has high Ψ_6 order parameter at H* = 1.9. For COs, both narrow-slit and flat-interface constraints lead to the formation of a hexagonal rotator phase (H_R) as well as a rhombic phase, which in our case is also buckled (due to the extra space along the Z axis). For TOs under flat-interface constraints, a hexagonal rotator (H_R) phase is seen, which leads to a rhombic phase upon further compression. In our case, we see a similar phase behavior with H_P, H_T and B_R phases, all of which show 6-fold bonding symmetry. We also note that experiments of interfacial self-assembly of nanoparticles with a cantellated cube shape (approaching a rhombicuboctahedron) have detected the formation of a buckled phase with octahedral symmetry[55].

5 Conclusions

We investigated the phase behavior of four representative polyhedral shapes from the truncated cube family, namely, cubes, TC4s, COs, and TOs, when confined inside a slit with hard walls separated a distance H*. The central aim was to explore the transitional phase behavior as the system goes from a quasi-2D geometry (for strong confinement, small H*) to a quasi-3D bulk behavior (for weak confinement, large H*). The choice of shapes was motivated by the growing availability of experimental methods that readily allow synthesis of nanoparticles with these shapes and by the theoretical and simulation studies that have predicted a rich bulk 3-D behavior for such systems.

While we found some common trends in all four shapes, there were aspects of their phase behavior that were unique to each particular shape. The common trends help us understand the generic effects of geometric confinement. We observed a saw-tooth-like pattern in the ordered-state densest packing as a function of H* that is associated with how efficiently the particles use the available space while accommodating some integer number of layers. The phase behavior is particularly interesting for monolayers as $H^* \rightarrow 2$, since the relatively large free space associated with the frustration of a second layer allows the possibility of alternative structures that can maximize entropy. Except for cubes, we detect the formation of buckled phases for all the other shapes within the range $1.5 < H^* < 2$. For the H* values we investigated, however, the phase

behavior does not converge to the bulk-3D behavior, although confinement effects weaken significantly for $H^* > 3$. As the asphericity in the shapes is reduced, our simulated phase diagrams show features that approach those of the phase behavior observed for hard spheres (HSs) in parallel-plate confinement[30]. Our simulated phase behavior for strong confinement (so that only a monolayer is allowed) also shows some similarities to that of freely rotating polyhedra whose centers of mass are confined to a flat surface[48]. All of our results are based on compression simulations only; complementary expansion runs were not performed as the densest packed configurations were unknown for most of the confinements of interest. Hence the phase boundaries outlined in this work are only approximate and some of the phases detected may even be metastable. However, they represent the most likely outcomes of typical particle confinement experiments that enact a gradual compression process akin to our simulation protocol. Our results could be further refined by identifying densest packed structures for varying confinement using, e.g., the Floppy Box Monte Carlo method[56].

The considerable effect of geometrical confinement on the phase behavior of truncated-cube type polyhedral nano- or micro-particles suggests that this provides an effective experimental route to engineer novel phases in these systems. Future studies could investigate how dynamic changes of the confinement may affect structure, assessing the robustness of some of the phases reported here and whether such changes could be coupled with phase transitions. Towards creating functional nanomaterials with tunable material properties, several strategies such as shape anisotropy, shape bi-dispersity, enthalpic 'patchy' particles are often used. Our work adds to the body of work that has shown that geometrical confinement can also effectively tune the particle structure and hence any structure-dependent property of interest.

Acknowledgements

Funding support is gratefully acknowledged from DOE (Office of Basic Energy Sciences, Division of Materials Sciences and Engineering under award Grant No. ER46517). The authors also thank Dr. U. Agarwal and V. Thapar for useful exchanges.

References

1 P. A. Buining, C. Pathmamanoharan, J. B. H. Jansen and H. N. W. Lekkerkerker, *Journal of the American Ceramic Society*, 1991, **74**, 1303–1307.
2 L. M. Liz-Marzan, M. Giersig and P. Mulvaney, *Langmuir*, 1996, **12**, 4329–4335.
3 O. Cayre, V. N. Paunov and O. D. Velev, *J. Mater. Chem.*, 2003, **13**, 2445–2450.
4 F. van der Kooij, K. Kassapidou and H. Lekkerkerker, *NATURE*, 2000, **406**, 868–871.
5 D. Dendukuri, D. C. Pregibon, J. Collins, T. A. Hatton and P. S. Doyle, *Nature materials*, 2006, **5**, 365–369.
6 C. J. Hernandez and T. G. Mason, *The Journal of Physical Chemistry C*, 2007, **111**, 4477–4480.
7 C.-Y. Chiu, Y. Li, L. Ruan, X. Ye, C. B. Murray and Y. Huang, *NATURE CHEMISTRY*, 2011, **3**, 393–399.
8 Y. Sun and Y. Xia, *Science*, 2002, **298**, 2176–2179.
9 O. C. Compton and F. E. Osterloh, *Journal of the American Chemical Society*, 2007, **129**, 7793–7798.
10 D. Seo, J. C. Park and H. Song, *Journal of the American Chemical Society*, 2006, **128**, 14863–14870.
11 B. S. John, C. Juhlin and F. A. Escobedo, *J. Chem Phys.*, 2008, **128**, 044909.
12 U. Agarwal and F. A. Escobedo, *Nature materials*, 2011, **10**, 230–5.
13 U. Agarwal and F. A. Escobedo, *J. Chem. Phys.*, 2012, **137**, 024905.
14 J. Henzie, M. Grünwald, A. Widmer-Cooper, P. L. Geissler and P. Yang, *Nature Materials*, 2012, **11**, 131–7.
15 P. F. Damasceno, M. Engel and S. C. Glotzer, *Science*, 2012, **337**, 453–457.
16 S. Torquato and Y. Jiao, *Nature*, 2009, **460**, 876–879.
17 J. H. Conway, Y. Jiao and S. Torquato, *Proceedings of the National Academy of Sciences*, 2011, **108**, 11009–11012.
18 Y. Jiao, F. H. Stillinger and S. Torquato, *Phys. Rev. E*, 2009, **79**, 041309.
19 J. de Graaf, R. van Roij and M. Dijkstra, *Phys. Rev. Lett.*, 2011, **107**, 155501.
20 P. Pieranski, *Phys. Rev. Lett.*, 1980, **45**, 569–572.
21 P. Pieranski, L. Strzelecki and B. Pansu, *Phys. Rev. Lett.*, 1983, **50**, 900–903.
22 D. H. Van Winkle and C. A. Murray, *Phys. Rev. A*, 1986, **34**, 562–573.
23 J. A. Weiss, D. W. Oxtoby, D. G. Grier and C. A. Murray, *The Journal of Chemical Physics*, 1995, **103**, 1180–1190.
24 S. Neser, C. Bechinger, P. Leiderer and T. Palberg, *Phys. Rev. Lett.*, 1997, **79**, 2348–2351.
25 I. Cohen, T. G. Mason and D. A. Weitz, *Phys. Rev. Lett.*, 2004, **93**, 046001.
26 I. Cohen, B. Davidovitch, A. B. Schofield, M. P. Brenner and D. A. Weitz, *Phys. Rev. Lett.*, 2006, **97**, 215502.
27 M. Schmidt and H. Löwen, *Phys. Rev. Lett.*, 1996, **76**, 4552–4555.
28 R. Zangi and S. A. Rice, *Phys. Rev. E*, 2000, **61**, 660–670.
29 R. Messina and H. Löwen, *Phys. Rev. E*, 2006, **73**, 011405.
30 A. Fortini and M. Dijkstra, *Journal of Physics: Condensed Matter*, 2006, **18**, L371.
31 E. C. Ouz, R. Messina and H. Lwen, *EPL (Europhysics Letters)*, 2009, **86**, 28002.
32 H. Löwen, *Journal of physics. Condensed matter : an Institute of Physics journal*, 2009, **21**, 474203.
33 M. Cosentino Lagomarsino, M. Dogterom and M. Dijkstra, *The Journal of Chemical Physics*, 2003, **119**, 3535–3540.
34 M. A. Bates and D. Frenkel, *The Journal of Chemical Physics*, 2000, **112**, 10034–10041.
35 K. W. Wojciechowski and D. Frenkel, *Comput. Methods Sci. Technol.*, 2004, **10**, 235–255.
36 C. Avendano and F. A. Escobedo, *Soft Matter*, 2012, **8**, 4675–4681.
37 S. Atkinson, Y. Jiao and S. Torquato, *Phys. Rev. E*, 2012, **86**, 031302.
38 C. Avendano, C. M. Liddell Watson and F. A. Escobedo, *Soft Matter*, 2013, **9**, 9153–9166.
39 B. de Nijs, S. Dussi, F. Smallenburg, J. D. Meeldijk, D. J. Groenendijk, L. Filion, A. Imhof, A. van Blaaderen and M. Dijkstra, *Nat Mater*, 2015, **14**, 56–60.
40 T. D. Clark, J. Tien, D. C. Duffy, K. E. Paul and G. M. Whitesides, *Journal of the American Chemical Society*, 2001, **123**, 7677–7682.
41 I. D. Hosein and C. M. Liddell, *Langmuir*, 2007, **23**, 10479–10485.

42 E. K. Riley and C. M. Liddell, *Langmuir*, 2010, **26**, 11648–11656.

43 E. Y. K. Fung, K. Muangnapoh and C. M. Liddell Watson, *J. Mater. Chem.*, 2012, **22**, 10507–10513.

44 E. K. Riley, E. Y. Fung and C. M. L. Watson, *Journal of Applied Physics*, 2012, **111**, –.

45 E. K. Riley and C. M. Liddell Watson, *Journal of Applied Physics*, 2014, **115**, –.

46 L. G. Cmara and F. Bresme, *The Journal of Chemical Physics*, 2004, **120**, 11355–11358.

47 A. P. Gantapara, J. de Graaf, R. van Roij and M. Dijkstra, *Phys. Rev. Lett.*, 2013, **111**, 015501.

48 V. Thapar, T. Hanrath and F. A. Escobedo, *Soft Matter*, 2015, **11**, 1481–1491.

49 M. R. Khadilkar and F. A. Escobedo, Electronic supplementary information (ESI) available. See DOI: (DOI to be inserted).

50 E. G. Golshtein and N. V. Tretyakov, *Modified Lagrangians and monotone maps in optimization*, New York- Wiley, 1996.

51 M. Mazars, *EPL (Europhysics Letters)*, 2008, **84**, 55002.

52 P. J. Steinhardt, D. R. Nelson and M. Ronchetti, *Phys. Rev. B*, 1983, **28**, 784–805.

53 F. Smallenburg, L. Filion, M. Marechal and M. Dijkstra, *Proceedings of the National Academy of Sciences of the United States of America*, 2012, **109**, 17886–17890.

54 V. Elser, *Phys. Rev. E*, 2014, **89**, 052404.

55 M. P. Boneschanscher, W. H. Evers, J. J. Geuchies, T. Altantzis, B. Goris, F. T. Rabouw, S. A. P. van Rossum, H. S. J. van der Zant, L. D. A. Siebbeles, G. Van Tendeloo, I. Swart, J. Hilhorst, A. V. Petukhov, S. Bals and D. Vanmaekelbergh, *Science*, 2014, **344**, 1377–1380.

56 L. Filion and M. Dijkstra, *Phys. Rev. E*, 2009, **79**, 046714.